

# Modulating grid cell scale and intrinsic frequencies via slow high-threshold conductances: a simplified model

Diogo Santos-Pata<sup>a,c</sup>, Riccardo Zucca<sup>a</sup>, Héctor López-Carral<sup>a</sup>, Paul F. M. J. Verschure<sup>a,b,c,\*</sup>

<sup>a</sup>*Institute for Bioengineering of Catalonia (IBEC),  
Barcelona Institute of Science and Technology (BIST), Barcelona, Spain*  
<sup>b</sup>*Institució Catalana de Recerca i Estudis Avançats (ICREA), Barcelona, Spain*  
<sup>c</sup>*Universitat Pompeu Fabra (UPF), Barcelona, Spain*

---

## Abstract

Grid cells in the medial entorhinal cortex (MEC) have known spatial periodic firing fields which provide a metric for the representation of self location and path planning. The hexagonal tessellation pattern of grid cells scales up progressively along the MEC's layer II dorsal-to-ventral axis. This scaling gradient has been hypothesized to originate either from inter-population synaptic dynamics as postulated by attractor networks, or from projected theta frequencies to different axis levels, as in oscillatory models. Alternatively, cellular dynamics, and specifically slow high-threshold conductances, have been hypothesized to have an effect in the scaling of grid cells. To test the hypothesis these intrinsic hyperpolarization-activated cation currents account for the scale gradient as well as the different oscillatory frequencies observed along the dorsal-to-ventral axis, we have modeled and analyzed data from a population of grid cells simulated with spiking neurons interacting through low-dimensional attractor dynamics. To investigate the causal relationship between oscillatory frequencies and grid scale increase, we analyzed the dominant frequencies of the membrane potential for cells with distinct after-spike dynamics. We observed that intrinsic neuronal membrane properties of simulated cells could induce an increase of grid scale when modulated by after-spike reset values. Differences in the membrane potential oscillatory frequency were observed along the simulated dorsal-to-

---

\*Corresponding author

*Email address:* [pverschure@ibecbarcelona.eu](mailto:pverschure@ibecbarcelona.eu) (Paul F. M. J. Verschure)

ventral axis, suggesting that, rather than driving to the increase of grid scale as proposed by interference models of grid cells, they are the result of intrinsic cellular properties of neurons at each axis level. Overall, our results suggest that the after-spike dynamics of cation currents may play a major role in determining the grid cells' scale and that oscillatory frequencies are a consequence of intrinsic cellular properties that are specific to different levels of the dorsal-to-ventral axis in the MEC layer II.

*Keywords:* grid cells, entorhinal, hyperpolarization, space

---

## 1 Introduction

Grid cells found in layer II of the medial entorhinal cortex (MEC) present multiple regularly-spaced firing fields organized in a triangular tessellation that spans the entire explored environment [1, 2]. Functionally, grid cells represent a spatial metric system signaling the position of the animal in the environment. Together with sensory cells in the lateral entorhinal cortex (LEC), grid cells in MEC layer II project to both the dentate gyrus (DG) and CA3 neurons of the hippocampus proper [3, 4]. Thus, the mammalian hippocampus robustly encodes spatial representation using a combination of environment-related spatial and sensory information.

Since the discovery of grid cells, several computational models have been proposed to describe the spatial and temporal properties of grid fields' formation. Most of the proposed models can be categorized into two groups: oscillatory interference [5] and attractor dynamics [6, 7] models. For the former group, the typically observed hexagonal grid pattern emerges from the interaction of multiple phase-synchronized oscillations that are based on the animal's speed vector projected to MEC layer II from earlier MEC layers. Thus, at the computational level, manipulating the amplitudes and phase differences of these oscillations modulates the scale of the resulting grid cells. On the other hand, in the attractor-based models, the distribution of synaptic weights within an all-to-all network creates a characteristic "bump" of activity that converges to stable attractor points. The network weights configuration is updated according to the spatial motion of the agent at every timestep ( $t$ ), which allows for the characteristic periodic firing across the explored environment. Recent studies on the intrinsic cellular properties of grid cells support the idea of low-dimensional continuous attractor dynamics

27 in the grid cells' system, favoring the computational principles of attractor-  
28 based models of grid cells [8, 9].

29 The size and spacing of grid cells' firing fields have been shown to increase  
30 progressively along the dorsal-to-ventral axis of the MEC [1, 10, 11]. Func-  
31 tionally, such a scale gradient has been suggested to operate as an accurate  
32 path-integration mechanism projecting to the DG and CA3 hippocampal  
33 sub-regions [10]. Moreover, the interaction between grid scales and other  
34 spatially tuned cells have been suggested to serve for minimizing errors in  
35 path integration [12].

36 Despite observations on hyperpolarization-activated cyclic nucleotide-gated  
37 (HCN) channels' disruption and its effects on grid scale [13], the mechanism  
38 underlying the differences in scale of such neural populations is still not clear.  
39 Different sub-threshold theta oscillatory frequencies have been measured in  
40 vitro in neurons along the dorsal-to-ventral axis, suggesting that individ-  
41 ual cells' intrinsic frequencies might play a key role on grid cells' scale [14].  
42 Moreover, it has been shown that the distance from the dorsal surface is  
43 accompanied by a decrease in oscillatory frequency in MEC layer II [15].

44 From the continuous attractor model perspective, different scales are often  
45 obtained by manipulating the variance of the Gaussian synaptic distributions.  
46 However, given recent insight on the effects of HCN channels disruption in  
47 grid cells' metrics, the distribution of synaptic weights might not be the main  
48 factor accounting for grid scale and stability of the network activity.

49 Coherent with such idea, previous computational models of grid cells [16]  
50 have explicitly pointed out that differences in grid cells' scale along the dorsal-  
51 to-ventral axis are linked to differences in the cells' intrinsic frequencies.

52 Indeed, a systematic topographical change in time constants of hyperpolarization-  
53 activated cation currents ( $I_h$ ) of stellate cells has been observed in vitro [14].  
54 Moreover, those topographical changes correlate with membrane potential  
55 oscillation frequency and differences in the time constant of the sag response.

56 This suggests that different  $I_h$  kinetics, which are regulated by the HCN fam-  
57 ily proteins, may play a critical role in the change of oscillatory frequencies  
58 along the dorsal-to-ventral axis and the topographical expansion of grid scale  
59 [15]. Forebrain-specific knockout of the HCN1 subcomponent in mice has  
60 been shown to selectively affect the Y-intercept of the grid scale, indicating  
61 that those elements of the HCN family are involved in grid scale modulation  
62 [13, 17].

63 Previous studies have addressed the question of how intrinsic cell's fre-  
64 quency affects the grid scale along the dorsal-to-ventral axis [18]. Specifi-

65 cally, they proposed a model where the addition of physiologically plausible  
66 after-spike dynamics modulates the observed increase in grid scale along the  
67 dorsal-ventral axis of MEC.

68 Whether the membrane potential oscillatory frequency is sufficient to  
69 determine the grid scale is still unclear. In attractor models of grid cells'  
70 formation, the scale of the grid is modulated by a gain parameter affecting  
71 the synaptic connectivity of the network and thus the speed at which the  
72 activity bump moves along the network as well [18, 19]. However, there is no  
73 biological evidence for such connectivity matrix discretization. In interfer-  
74 ence models, the differences in grid scale are generated due to amplitude and  
75 phase changes in the oscillatory inputs to the grid cells network. Despite the  
76 fact that differences in the oscillatory frequencies are observable in biological  
77 systems, it is not clear whether it emerges from intrinsic or extrinsic network  
78 dynamics. The fact that knocking out HCN family type genes disrupts the  
79 normal progressive scale increase raises the question as to whether such scale  
80 gradient is a network or a cellular property. We address this by presenting a  
81 simplified spiking computational model that describes the generation of the  
82 spatial and temporal properties of grid cells found in physiological studies.

## 83 2. Materials and methods

84 In order to explore the effects of intrinsic cellular properties on differences  
85 in spatial grid scale as seen in the dorsal-to-ventral axis of MEC layer II and  
86 the influence on the oscillatory frequency at each axis level, we created a  
87 simulated environment where a virtual agent was randomly exploring either  
88 a one-dimensional linear track or a two-dimensional square arena (see Fig. 1).  
89 In both environments, the agent's speed vector is fed as the input to an  
90 ensemble of simulated neuronal populations (which we describe below).

91 In line with Yoon et al. [9] observations of low-continuous attractor dy-  
92 namics in grid cells' populations, we built on elements of a previously pre-  
93 sented grid cells model based on attractor dynamics [19] and translated it  
94 to a spiking neuronal model, approximating the spiking behavior observed  
95 in MEC layer II stellate cells. A total of 19 populations of grid cells were  
96 included in the model, each containing 100 neurons connected in an *all-to-all*  
97 fashion (Fig. 1A). Recordings from large ensembles of grid cells in individual  
98 rats have suggested that MEC layer II modules are functionally and anatom-  
99 ically discrete and independent from each other [11]. Building upon such

100 observations, we assumed no synaptic connectivity between cells belonging  
 101 to the different populations.

102 At the topological level, the network is based on the twisted toroidal  
 103 architecture (Fig. 1E) and synaptic weights are dependent on the Cartesian  
 104 distance of each cell to its postsynaptic cells and updated according to the  
 105 input provided by the speed vector of the simulated agent moving within the  
 106 virtual environment ( (Fig. 1E) and [19] for more details).

107 Given our aim to clarify the functional role of HCN-channels in modu-  
 108 lating grid scale, we isolated the simulated grid cell populations from other  
 109 anatomically connected brain regions, such as earlier MEC layers. There-  
 110 fore, apart from the injection of a current to initialize the model, there was  
 111 no further afferent signal input throughout the simulations. Nevertheless,  
 112 due to the recurrent connectivity nature of the network topology, as well as  
 113 the changing in synaptic distribution depending on the simulated agent’s dis-  
 114 placement, individual cells were susceptible of firing, as observed in previous  
 115 models [31].

116 MEC layer II stellate cells were modelled using the simplified Izhikevich’s  
 117 spiking model [22]. Such a model allows for the direct manipulation of the  
 118 resonant properties affected by HCN channels in biological stellate cells [13]  
 119 through a single parameter. Parameters values were selected to reproduce  
 120 the characteristic bursting behavior of MEC layer II grid cells observed ex-  
 121 perimentally in stellate cells recordings [22, 23, 24]. The activation function  
 122 of each neuron in the network was defined by a system of ordinary differential  
 123 equations given by:

$$dv/dt = 0.04v^2 + 5v + 140 - u + I \quad (1)$$

$$du/dt = a(bv - u) \quad (2)$$

124 where  $0.04v^2 + 5v + 140$  mimics the spike initiation dynamics of a neuron,  
 125  $I$  represents synaptic currents or injected DC-currents,  $v$  represents the cell’s  
 126 membrane potential and  $u$  describes the membrane recovery variable.  $a$  de-  
 127 scribes the time scale of the recovery variable  $u$  and  $b$  describes the sensitivity  
 128 of the recovery variable  $u$  to the subthreshold fluctuations of the membrane  
 129 potential  $v$ .

130 The after-spike resetting mechanism is given by:

$$\text{if } v \geq 30 \text{ mV, then } \{ v \leftarrow cu \leftarrow u + d \quad (3)$$

131 where  $c$  and  $d$  describe the after-spike membrane value and recovery vari-  
132 able, respectively.

133 To test whether the modulation of HCN channels is sufficient to trigger  
134 changes in grid cells' scale, the after-spike reset value of cation currents  $d$   
135 was varied across populations in the range 0.2 - 3.8 mV/ms with linearly  
136 increasing steps (Fig. 1B). The parametric space was defined in order to  
137 maintain the spiking behavior of stellate cells (Fig. 1C-D). All the other  
138 model parameters were kept constant over all the neuronal populations.

139 The parameter  $a$ , which describes the cell's current recovery variable time  
140 scale, was set to 0.03. The parameter  $b$ , describing the cell's current recovery,  
141 was set to 0.2. The parameter  $c$ , describing the after-spike reset value of the  
142 cell's membrane potential, was set to -50 mV. The spike train activity of each  
143 cell was recorded and used for the subsequent analysis.

144 The virtual agent's method of exploration was set to exhibit two different  
145 behaviors depending on the environment. In order to analyze differences in  
146 periodicity and size of grid cells' firing fields for populations with different  
147  $I_h$  currents, the first behavior of the agent was to run back-and-forth in a  
148 linear track environment. For the second environment, the square arena, the  
149 agent would explore the arena randomly. Thus, in the second environment,  
150 the characteristic 2D rate maps of grid cells can be depicted.

151 Simulations were initialized with grid cells receiving an external current  
152 input sampled from a uniform random distribution with mean 5.0. The main  
153 input of the network is the speed vector  $s$  of the agent's translation at each  
154 time step. This input is independent on any absolute information about  
155 animal's location.

156 Previous computational models of grid cells relied on a subset of neurons  
157 encoding for distinct head-orientations to modulate the activity bump dis-  
158 placement along the neural sheet [32]. In our model, the network's weight  
159 distribution is reliant on the speed vector of the simulated agent's displace-  
160 ment,  $s := (s_x, s_y)$ , allowing the activity bump of the network to drift along  
161 the neural sheet when the agent moves according to its speed vector. Even  
162 though there is no evidence for synaptic modulation at such short temporal  
163 intervals in biological systems, we used such method (as described in [19]) to  
164 abstract direction tuned grid cells as in [32].

165 Whereas in the original grid cell model proposed by [19] the speed vector  
166  $s$  is susceptible of modulation via a gain parameter, affecting the grid scale, in  
167 our simulations, the speed vector was kept constant throughout the simulated  
168 conditions.

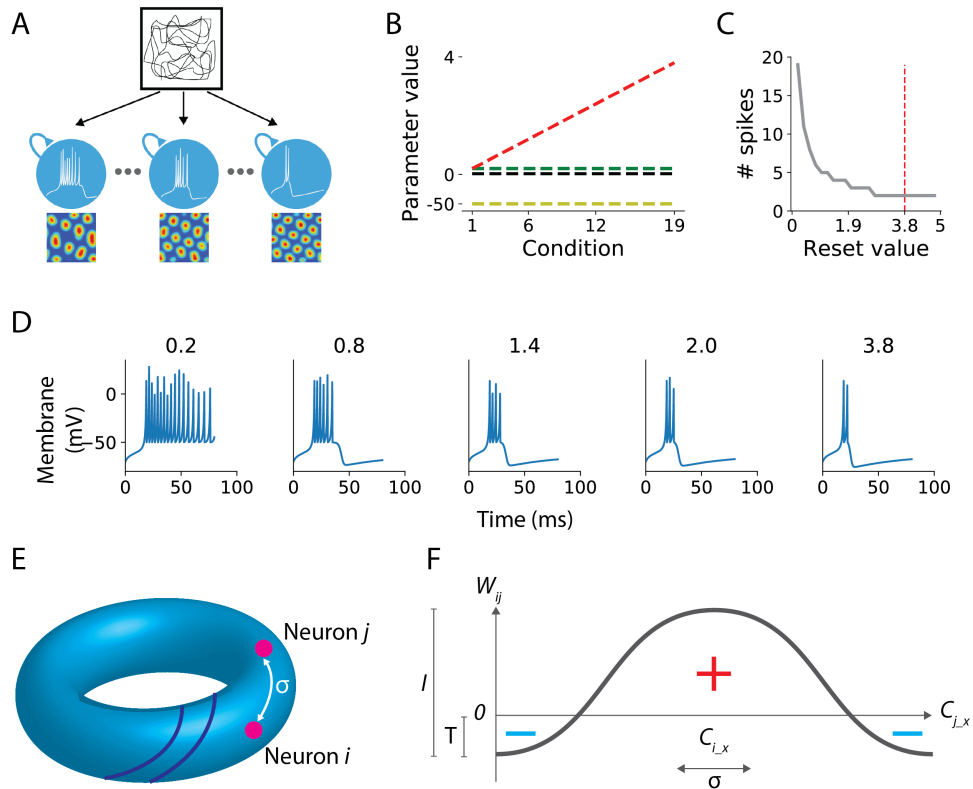


Figure 1: **Illustrative description of the methods used in this study.** **A.** A virtual agent is set to randomly explore a squared virtual arena. During exploration, 19 different populations of grid cells are activated and all receive inputs from the vestibular system encoding the speed vector of the virtual agent. Each population of grid cells was initialized with specific cell model parameters as shown in B. The spatial rate map of each cell belonging to each population was stored for further analysis. **B.** Izhikevich model parameters used per each population (condition). Every parameter value was kept constant for every population, with the exception of the  $d$  parameter ranging from 0.2 to 3.8 in steps of 0.2. **C.** Number of spikes as a function of the  $d$  parameter. With all the other cell's parameters maintained constant a plateau is observed for reset values larger than 3. **D.** Simulations of hippocampal stellate neurons for the 19 populations included in the model by varying the  $d$  parameter. **E.** 3-dimensional representation of the model topology based on the twisted-toroidal synaptic distribution. Note the 2 dark-blue lines illustrating twist and how the Cartesian distance ( $\sigma$ ) between neuron  $i$  and neuron  $j$  modulates their synaptic strength. **F.** Synaptic weights  $W_{ij}$  implemented in the current model are modulated by the Cartesian distance ( $\sigma$ ) between neurons in the neural lattice.

169 The synaptic weights distribution was defined as:

$$w_{ij}(t) = I * \exp\left(-\frac{\|c_i - c_j + s(t)\|_{tri}^2}{\sigma^2}\right) - T \quad (4)$$

170 where  $\|c_i - c_j\|_{tri}^2$  denotes the Cartesian distance between cells  $c_i$  and  $c_j$   
171 in the network matrix,  $I$  ( $= 0.3$ ) defines the synaptic strength,  $\sigma$  ( $= 0.48$ )  
172 modulates the width of the synaptic weight distribution and  $T$  ( $= 0.05$ ) is  
173 the excitatory and inhibitory distance threshold.

### 174 *2.1. Data analysis*

175 The model was implemented using NEST neural networks simulator [20],  
176 and all the analyses were done using the SciPy python scientific library [21].  
177 Occupancy maps were calculated as the total time an agent spent in each  
178 spatial bin ( $50 \times 50$  pixels) within the virtual arena. Rate maps were then  
179 obtained by normalizing each cell's spiking activity within a spatial bin with  
180 the agent's occupancy map. Autocorrelograms were then obtained by the  
181 spatial autocorrelation of the rate map of each cell in the 2-dimensional  
182 plane.

183 Frequency analyses were obtained by averaging the dominant frequency  
184 provided by the power spectral density (PSD). To compute the dominant  
185 membrane potential oscillation frequency, continuous, contiguous and non-  
186 overlapping windows of 10 seconds were extracted from each cell membrane  
187 potential and their PSD was computed. The second highest peak of the  
188 averaged PSD was considered the dominant frequency for a given cell.

189 An Ipython notebook with the complete model's code is available at the  
190 following repository: <https://osf.io/w96fq/>.

## 191 **3. Results**

192 To verify that the manipulation of the intrinsic cellular properties in the  
193 chosen cell model simulation would not affect the attractor mechanism of  
194 the networks, we set every simulation to be a random state of activity and  
195 visually ensured that an activation bump was formed and remained stable  
196 throughout the virtual agent navigation. The formation of the activity bump  
197 during the initial simulation steps for three representative populations with  
198 different after-spike reset values are shown in Fig. S1.



199 3.1. Grid scale is modulated by  $I_h$

200 3.1.1. Linear track simulation

201 The virtual agent was set to run along a linear track environment, mea-  
202 suring 200 virtual units, at a constant speed of 20 virtual units/second. A  
203 total of 1900 spike trains were recorded.

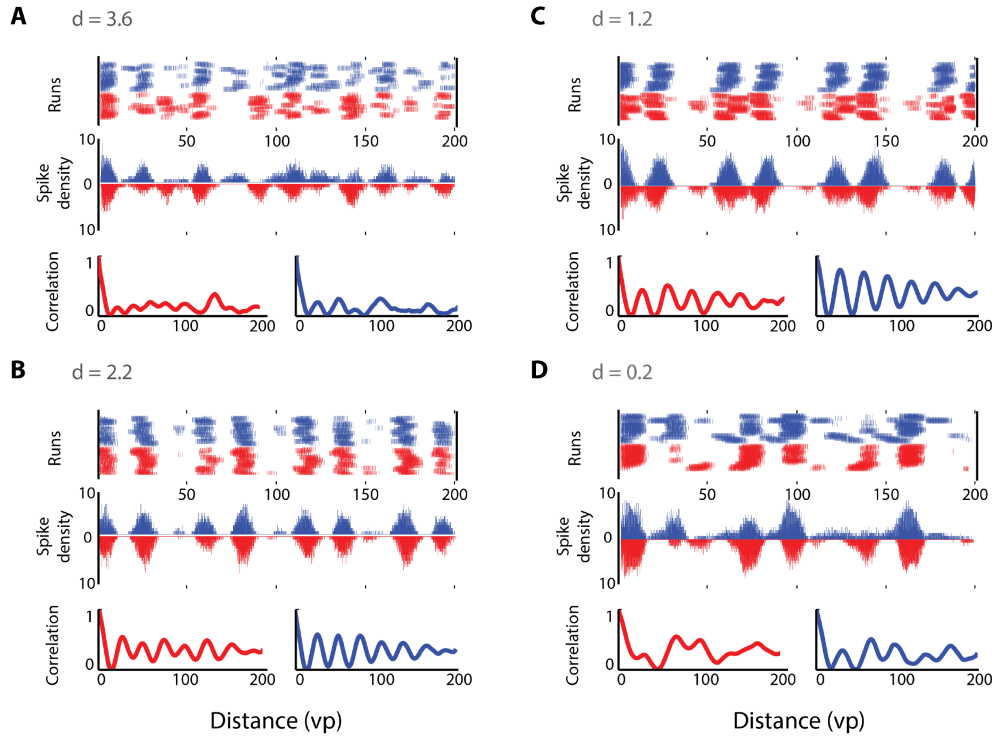


Figure 2: **Progressive increase in grid scale from dorsal to ventral MEC.** Spike-trains of four representative cells from dorsal (A) to ventral (D) axis populations. Left trajectories (red) and right trajectories (blue) are differentiated. Top subplots represent the raw spikes against the position of the linear track per each run. Middle subplots represent the spike density per position (same color code as in top plot). Bottom subplots show the correlations of spike density along the linear track. Higher to lower oscillation of spike density and correlation is observed from dorsal to ventral levels.

204 To test whether the modulation of HCN channels is sufficient to trigger  
205 changes in grid cells' scale, the after-spike reset values of cation currents  
206  $d$  were varied across populations. Fig. 2 illustrates the effects of varying

207 the after-spike dynamics on the firing fields of 4 representative cells from  
 208 the simulated dorsal-to-ventral axis level conditions ( $d = 3.6, 2.2, 1.2, 0.2$ ).  
 209 Within the linear track, spike activity relative to the agent’s position in the  
 210 environment points to an increase in firing-fields size and distance that is  
 211 dependent on the value of  $d$ . The effect appears more evident from the  
 212 spike density plots (Fig. 2 middle subplots) and by the periodic regions of  
 213 high activity observed in the spike density autocorrelations (Fig. 2 bottom  
 214 subplots).

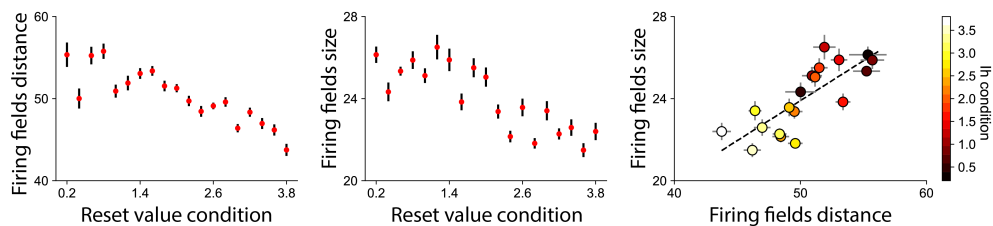


Figure 3: **Grid field sizes and spatial distance in simulations run with varying after-spike-reset values.** Firing field distance (**left**) and size (**center**) decrease along the simulated conditions for larger  $d$ . **left** Together, firing fields size and distance are tightly correlated and modulated by  $I_h$  values. Data points represent the average  $\pm$  SD of all cells in a simulated neuronal population.

215 To quantify the increase in grid scale at the population level, we have  
 216 quantified each simulated cell firing field’s size and distance (Fig. 3). To do so,  
 217 we obtained the firing rate, spike count, at each position of the linear track as  
 218 in Fig. 2 (bin size = 5 virtual points). A peak detection algorithm was applied  
 219 to identify the firing fields. Firing fields whose peak rate was larger than 1.2  
 220 standard deviations (z-scored) were included in the sample and the averaged  
 221 distance between consecutive fields of each cell was computed. Increasing the  
 222 hyperpolarization reset value  $d$  caused a decrease in the averaged firing field  
 223 distance (Pearson  $r = -0.34, p < 0.01$ , Fig. 3-top left). Similarly, in order to  
 224 quantify each cell’s firing field size, we obtained the spatial distance between  
 225 the two firing rate points on each side of its peak whose first derivative was  
 226  $\geq 0$ . As for distance, we found that firing fields size is negatively modulated  
 227 by the after-spike reset parameter (Pearson  $r = -0.31, p < 0.01$ , Fig. 3-top  
 228 right). We next asked whether firing fields size and distance were equally  
 229 affected by the hyperpolarization reset value of each condition. To do so, we  
 230 averaged firing fields size and distance of cells belonging to the same condition

231 (Fig. 3-bottom). A strong correlation between size and distance revealed  
 232 significance (Pearson  $r = 0.79, p < 0.01$ ). Moreover, the increase in these  
 233 spatial measures was accompanied by a decrease in the hyperpolarization  
 234 reset value (see  $I_h$  condition in Fig. 3-bottom, colorbar).

235 Further, we analyzed the relationship between the size and the distance  
 236 of the firing fields of every cell used in our simulations with the hyperpo-  
 237 larization reset value of each condition through a generalized linear model  
 238 (GLM). According to the output, firing field size was modeled accordingly  
 239 by:  $\text{logit}(\pi_i) = 5.3 - 0.1 * \text{size}$ , and  $\text{variance} = 0.019$ . Firing field dis-  
 240 tance was modeled accordingly by:  $\text{logit}(\pi_i) = 6.6 - 0.07 * \text{distance}$ , and  
 241  $\text{variance} = 0.012$ .

### 242 3.1.2. 2D arena simulation

243 With the linear track simulations, we have shown that the intrinsic prop-  
 244 erties of grid cells can effectively modulate firing field size and spacing. How-  
 245 ever, testing such grid cell properties in a linear trajectory could fail to  
 246 demonstrate possible deformations in the characteristic grid pattern.

247 In order to observe the stereotypical pattern of grid cell and the accounts  
 248 of after-spike hyperpolarization behavior in grid resolution, we have set the  
 249 virtual agent to perform random exploration within a two-dimensional open  
 250 field arena. Similar to the 1D runs, we recorded the membrane potentials of  
 251 stellate cells belonging to different simulated dorsal-to-ventral axis levels. As  
 252 expected, the firing properties of cells at the ventral level presented larger and  
 253 further distributed firing-fields when compared with the ones at the dorsal  
 254 level (Fig. 4)

255 In order to quantify the stability of our model in the grid cells' spatial  
 256 representation, we used the gridness score measure for every cell's autocor-  
 257 relogram using correlations of rotational symmetry [25], by comparing the  
 258 spatial autocorrelation maps to the rotated versions of themselves with  $30^\circ$   
 259 rotations as:

$$G_S = \min(A_{\text{corr}60^\circ}, A_{\text{corr}120^\circ}) - \max(A_{\text{corr}30^\circ}, A_{\text{corr}90^\circ}, A_{\text{corr}150^\circ}) \quad (5)$$

260 Overall, rate maps along the simulated conditions revealed to be in the  
 261 range of gridness scores observed in tessellation patterns activity ( $> 0.15$ ) and  
 262 were not affected by the hyperpolarization reset value (Pearson  $r = 0.061, p =$   
 263  $0.23$ ), suggesting a stable spatial representation across the simulated dorsal-  
 264 to-ventral axis.

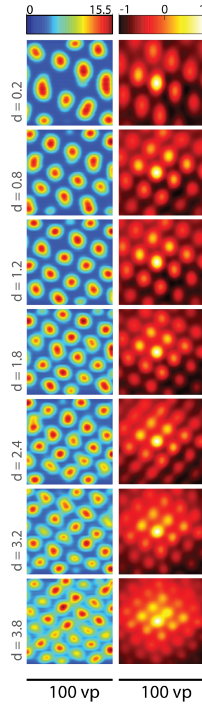


Figure 4: **Single cell's rate maps and autocorrelograms of neurons along dorsal-to-ventral axis.** Cell's spatial activity from ventral (top) to dorsal (bottom) axis level. Hyperpolarization-reset value represented by  $d$  at left most side. Progressively decrease of grid cell scale (left column), accompanied by its autocorrelogram (right column).

265 In order to quantify for differences along dorsal-to-ventral levels, we have  
 266 correlated membrane potentials of cells within each module. Lags calculated  
 267 after correlating membrane potential signals were taken as a measure of the  
 268 periodic increase in the amplitude of cells firing rate. Thus, high-resolution  
 269 grid cell rate-maps at the dorsal level (smaller scale) should reveal shorter  
 270 distances between firing fields and larger distances for the ones at the ven-  
 271 tral level (larger scale). As expected, we observed a progressive decrease  
 272 in membrane potential autocorrelations lags as a function of the after-spike  
 273 parameter (Pearson  $r = -0.94$ ,  $p < 0.01$ , Fig. 5-right). As grid cell hexag-  
 274 onal tessellation patterns and membrane potentials are not dissociable, we  
 275 have also quantified spatial lags in between firing fields. As for membrane  
 276 potentials, lags between spatial firing-fields were larger for smaller hyper-

277 polarization reset values (Pearson  $r = -0.91$ ,  $p < 0.01$ , Fig. 5-left) as well  
 278 as for rate maps spatial auto-correlation (Pearson  $r = -0.96$ ,  $p < 0.01$ ,  
 279 Fig. 5-middle). Fig. S2 further illustrates pairwise distances between spatial  
 280 observations.

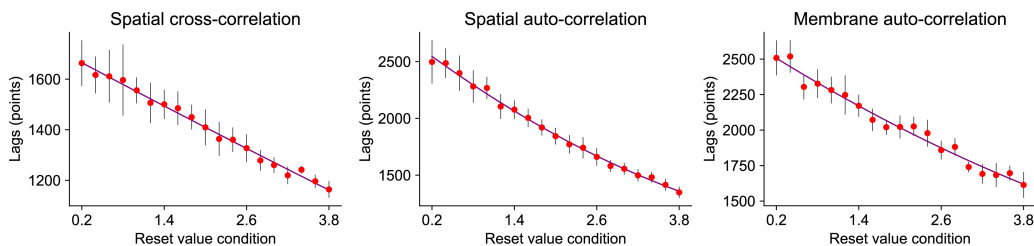


Figure 5: **Spatial correlation lags from spike-train and membrane potential along dorsal-to-ventral axis.** Lags of correlation along most ventral (0.2) to most dorsal (3.8) conditions. Left and middle plots represent lags of cross- and autocorrelation from 10 cells at each condition. Right plot represents the lags of autocorrelation for membrane potential of each cell. Increase of hyperpolarization-reset value is accompanied by the decrease of lags from ventral to dorsal axis locations.

281 Despite spatial grid-cell scale distribution found along the dorsal-to-ventral  
 282 axis levels of MEC layer II, the oscillatory properties of stellate grid cells are  
 283 also organized on the same axis [10, 18]. To verify whether the hyperpolar-  
 284 ization behavior accounting for the spatial resolution organization was also  
 285 sufficient to modulate the dominant frequencies of simulated neurons, we  
 286 have compared dominant frequencies of cells at multiple dorsal-to-ventral  
 287 axis modules. As in [10], dominant frequencies were observed to decrease  
 288 from dorsal to ventral modules, ranging 14-22 Hz (Pearson  $r = 0.45$ ,  $p <$   
 289  $0.01$ , Fig. 6-left). Note that frequencies are not in a theta range as ex-  
 290 pected in MEC, which could be due to the absence of inhibitory projec-  
 291 tions either from within the MEC population or arriving from hippocampus  
 292 proper feedback projections. However, there is evidence that modulation of  
 293 hyperpolarization-after values is sufficient to explain a decrease of membrane  
 294 potential frequency from dorsal to ventral levels. Thus, spatial scale and os-  
 295 cillatory frequency might be explained by the intrinsic cell hyperpolarization  
 296 mechanism.

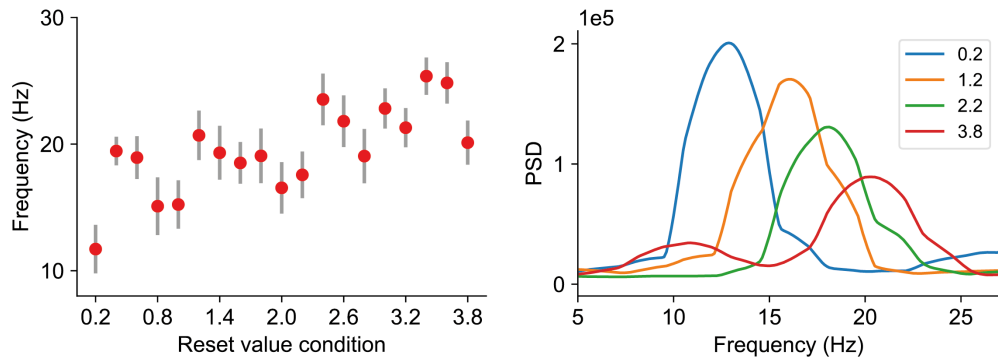


Figure 6: **Increase of dominant frequencies from ventral (left) to dorsal (right).**

297 **Discussion**

298 Grid cells in MEC layer II have been characterized by their grid scale,  
 299 which progressively increases along the dorsal-to-ventral axis. So far, grid  
 300 cells’ computational models either use oscillatory interference or attractor-  
 301 based dynamics to elicit the desired behaviors. Hybrid models have also been  
 302 proposed [26]. Regardless, the mathematical formulation to modulate grid  
 303 scale has been attributed to network dynamics, in the case of attractor-based  
 304 models, and to network inputs, in the case of interference-based models. In-  
 305 terference models affect its grid cell scale by modulating the frequency of  
 306 oscillatory signals being projected to the ensemble of grid cells in the net-  
 307 work [5]. Attractor dynamics-based grid cell models affect grid cells scale by  
 308 modulating the gain parameter which reflects how fast the bump of activity  
 309 in the network is translated to neighbor cells [19]. Even though both cate-  
 310 gories of grid cell models use network parameters to affect the grid cell scale,  
 311 it is still unclear what is modulating grid cells’ scale in the hippocampus.

312 Based on the findings by Giacomo et al. [14, 27], in this study, we hypoth-  
 313 esized that grid cells’ scale could be modulated exclusively through intrinsic  
 314 single-cell properties instead of network properties. To test our hypothesis,  
 315 we have built upon a previously presented model for grid cells formation  
 316 based on attractors dynamics [19], as has recently been observed in such  
 317 cell type [8, 9]. We used spiking neurons to mimic the properties of stellate  
 318 grid cells and thus modulate their hyperpolarization behavior. We found  
 319 that after-spike-reset scalars are sufficient to affect both the size and scale

320 of grid cells at different axis levels in the medial entorhinal cortex layer II.  
321 Specifically, we observed changes in the firing fields' size and scale, and their  
322 respective autocorrelation periodicity bumps from different after-spike-reset  
323 values conditions for linear track simulations.

324 Contrary to Brun et al. [10], we found periodic activity events for the  
325 population vector activity analysis. Indeed, one should argue that grid cell  
326 periodicity must be observed at the population level and, thus, whether such  
327 a phenomenon is accounted for in a living organism might depend on higher-  
328 level spatial encoding mechanisms such as environmental compartmentaliza-  
329 tion [28].

330 Because wild rodents typically navigate within two-dimensional environ-  
331 ments, we have also tested our model in a virtual agent moving in a 2D  
332 arena. As in the 1D environment, the agent had no spatial target position or  
333 goal and moved at random within the squared arena. Again, the attractor-  
334 based network was set to form grid cells as in Guanella et al. [19] using  
335 the Izhikevich neuron model [22] to mimic stellate cells found in MEC layer  
336 II. The only parameter differing among cells was the after-spike-reset val-  
337 ues specific to each sub-population. As expected, the size and scale of grid  
338 cells firing fields increased progressively across the simulated MEC layer II  
339 dorsal-to-ventral axis. Also, 2D navigation simulations allow us to confirm  
340 that gridness remained stable and was not affected by hyperpolarization re-  
341 lated properties. Linear decays along simulated conditions were observed for  
342 both spatial and membrane potential correlations lag, allowing the quantifi-  
343 cation of firing-fields distances.

344 In accordance with Brun et al. [10] and as hypothesized by Navratilova et al.  
345 [18], both oscillatory frequencies and spatial scale were affected by cellular  
346 after-spike-reset parameters, suggesting that biophysical mechanisms alone  
347 are sufficient to modulate multiple grid cell properties.

348 The flexibility of the synaptic connections has been previously questioned  
349 and marked as an implausible mechanism to update the attractor activity  
350 bump in the biological brain (McNaughton, 2006). One possibility to over-  
351 come such constraint was also discussed in the same paper (McNaughton,  
352 2006), with the solution to rely on multiple networks of conjunctive cells  
353 whose activity is dependent on the animal motion. On the other hand, slower  
354 mechanisms of synaptic matrix changes might compromise the efficacy of the  
355 model.

356 We have addressed the question of whether MEC layer II grid cell scale  
357 was determined by the network synaptic connectivity distribution, as pre-

358 dicted by low-continuous attractor models, or whether intrinsic properties  
359 of stellate cells accounting for individual cell’s hyperpolarization behavior  
360 was sufficient to modulate the rate-map resolution of explored environments.  
361 Our results suggest that biophysical grid-cell properties may be responsible  
362 for their spatial scale.

363 Despite the computational evidence, it is still not clear what are the  
364 mechanisms determining the differences in cells response across the dorsal-  
365 to-ventral axis level. During development, dorsal regions mature earlier than  
366 the ones at ventral levels [29]. Similarly, as the animal’s development ad-  
367 vances, so does its spatial exploration, covering more extensive regions of the  
368 environment. Thus, it is still uncertain as to what are the causal relation-  
369 ships between behavioral components of exploration, such as the magnitude  
370 of environmental exploration, and cellular development and organization. In  
371 this line, the work of [14] presented differences in the frequency of subthresh-  
372 old membrane potential oscillations in entorhinal cells. Moreover, in [13], the  
373 authors observed a modulation of the cell’s spatial scale in nucleotide-gated  
374 (HCN) channels knockout mice compared to sham, which suggests a func-  
375 tional role for HCN in mediating the topographic organization of firing fields  
376 in the explored environment.

377 Although only excitatory cells have been used in our implementation, the  
378 low-continuous attractor mechanism defines the synaptic weight between cells  
379 accordingly to their Cartesian distance in the neural sheet in a range from  
380 strong excitation to neighboring cells to strong inhibition to further apart  
381 cells. Excitation and inhibition projections from the same neuron is defi-  
382 nitely implausible in biological brains, however, that could be solved compu-  
383 tationally by setting the synaptic weights to the excitatory range and adding  
384 a population of inhibitory interneurons mediating neuronal competition, as  
385 suggested by the E%-max winner-take-all mechanism of gamma frequencies  
386 (de Almeida et al., 2009)

387 Along those lines, our work proposes specific physiological and develop-  
388 mental questions that could be tested experimentally. Specifically, character-  
389 ization of the bursting behavior observed in entorhinal stellate cells along the  
390 dorsal-ventral axis, as well as optogenetic stimulation modulating the neu-  
391 ron’s oscillatory dynamics could, potentially, support our modeling results.  
392 Moreover, at the computational level, this study proposes future work to un-  
393 veil the interactions between attractor dynamics and intrinsic properties of  
394 stellate cells in the MEC layer II.

395 In the presented form, our model served as an attempt to test the effects



396 of cell-specific spiking behavior in governing grid cell scale. As is, the cur-  
397 rent implementation allows testing hypothesis concerned with the individual  
398 dynamics of precise activity in such population as, for instance, spike-time  
399 dependent plasticity processes [33] or membrane-related contributions on net-  
400 work activity modulation. However, in doing so, this spiking implementa-  
401 tion of grid cells increases the difficulty to integrate and test the interplay  
402 between multiple brain regions involved in spatial representation [34]. In-  
403 deed, one limitation of our model is the absence of spatially tuned signals  
404 contributing to grid-cell stabilization [12]. Similarly, in our simulations, the  
405 spiking activity grid cells was modulated by, but did not contribute to, the  
406 agents displacement in the environment. Nevertheless, the learning dynamics  
407 of the navigational system have been observed to contribute to overt behav-  
408 ior during spatial decision making in both rodents [35] and humans [36]. To  
409 cope with such limitations, our model could, in future work, benefit from the  
410 recent advances in the development of brain-inspired artificial intelligence  
411 (BI-AI) systems to enhance our understanding of how these networks con-  
412 tribute, generate and maintain internal representations of spatial location in  
413 biological systems [30].

## 414 Acknowledgments

415 *Funding* The research leading to these results has received funding from  
416 the European Unions Horizon 2020 research and innovation programme under  
417 grant agreement No 826421 and No 820742.

## 418 References

- 419 [1] M. Fyhn, S. Molden, M. P. M. Witter, E. I. Moser, M.-B. Moser, Spa-  
420 tial representation in the entorhinal cortex., *Science* (New York, N.Y.)  
421 305 (August) (2004) 1258–64 (2004). doi:10.1126/science.1099901.
- 422 [2] T. Hafting, M. Fyhn, S. Molden, M.-B. Moser, E. I. Moser, Microstruc-  
423 ture of a spatial map in the entorhinal cortex., *Nature* 436 (7052) (2005)  
424 801–806 (2005). doi:10.1038/nature03721.
- 425 [3] N. M. van Strien, N. L. M. Cappaert, M. P. Witter, The anatomy of  
426 memory: an interactive overview of the parahippocampalhippocampal  
427 network, *Nature Reviews Neuroscience* 10 (4) (2009) 272–282 (2009).  
428 arXiv:9809069v1, doi:10.1038/nrn2614.

- 429 [4] E. I. Moser, Y. Roudi, M. P. Witter, C. Kentros, T. Bonhoeffer, M.-B.  
430 Moser, Grid cells and cortical representation, *Nature Reviews Neuro-*  
431 *science* 15 (7) (2014) 466–481 (2014). doi:10.1038/nrn3766.
- 432 [5] N. Burgess, C. Barry, J. O’Keefe, An oscillatory interference model  
433 of grid cell firing, *Hippocampus* 17 (9) (2007) 801–812 (2007).  
434 arXiv:NIHMS150003, doi:10.1002/hipo.20327.
- 435 [6] M. C. Fuhs, D. S. Touretzky, A spin glass model of path integration  
436 in rat medial entorhinal cortex, *Journal of Neuroscience* 26 (16) (2006)  
437 4266–4276 (2006). doi:10.1523/JNEUROSCI.4353-05.2006.
- 438 [7] B. L. McNaughton, F. P. Battaglia, O. Jensen, E. I. Moser, M. B. Moser,  
439 Path integration and the neural basis of the ‘cognitive map’, *Nat Rev*  
440 *Neurosci* 7 (8) (2006) 663–78 (2006). doi:10.1038/nrn1932.
- 441 [8] C. Domnisoru, A. A. Kinkhabwala, D. W. Tank, Membrane po-  
442 tential dynamics of grid cells, *Nature* (2013). arXiv:NIHMS150003,  
443 doi:10.1038/nature11973.
- 444 [9] K. Yoon, M. A. Buice, C. Barry, R. Hayman, N. Burgess, I. R. Fiete,  
445 Specific evidence of low-dimensional continuous attractor dynamics in  
446 grid cells, *Nature Neuroscience* (2013). doi:10.1038/nn.3450.
- 447 [10] V. H. Brun, T. Solstad, K. B. Kjelstrup, M. Fyhn, M. P. Witter, E. I.  
448 Moser, M.-B. Moser, Progressive increase in grid scale from dorsal to  
449 ventral medial entorhinal cortex, *Hippocampus* 18 (12) (2008) 1200–  
450 1212 (2008).
- 451 [11] H. Stensola, T. Stensola, T. Solstad, K. Frøland, M.-B. Moser, E. I.  
452 Moser, The entorhinal grid map is discretized., *Nature* 492 (7427) (2012)  
453 72–8 (2012). doi:10.1038/nature11649.
- 454 [12] D. Santos-Pata, R. Zucca, S. C. Low, P. F. M. J. Verschure, Size  
455 matters: How scaling affects the interaction between grid and border  
456 cells, *Frontiers in Computational Neuroscience* 11 (2017) 65 (2017).  
457 doi:10.3389/fncom.2017.00065.
- 458 [13] L. M. Giocomo, S. A. Hussaini, F. Zheng, E. R. Kandel, M. B. Moser,  
459 E. I. Moser, Grid cells use HCN1 channels for spatial scaling, *Cell* (2011).  
460 doi:10.1016/j.cell.2011.08.051.

- 461 [14] L. M. Giocomo, E. A. Zilli, E. Fransen, M. E. Hasselmo, Tem-  
462 poral Frequency of Subthreshold Oscillations Scales with Entorhi-  
463 nal Grid Cell Field Spacing, *Science* (2007). arXiv:NIHMS150003,  
464 doi:10.1126/science.1139207.
- 465 [15] L. M. Giocomo, M. E. Hasselmo, Time Constants of h Cur-  
466 rent in Layer II Stellate Cells Differ along the Dorsal to Ventral  
467 Axis of Medial Entorhinal Cortex, *Journal of Neuroscience* (2008).  
468 doi:10.1523/JNEUROSCI.3196-08.2008.
- 469 [16] J. O’Keefe, N. Burgess, Dual phase and rate coding in hippocampal place  
470 cells: Theoretical significance and relationship to entorhinal grid cells,  
471 *Hippocampus* 15 (7) (2005) 853–866 (2005). doi:10.1002/hipo.20115.
- 472 [17] D. L. Garden, P. D. Dodson, C. O’Donnell, M. D. White, M. F. Nolan,  
473 Tuning of synaptic integration in the medial entorhinal cortex to the  
474 organization of grid cell firing fields, *Neuron* 60 (5) (2008) 875 – 889  
475 (2008). doi:https://doi.org/10.1016/j.neuron.2008.10.044.
- 476 [18] Z. Navratilova, L. M. Giocomo, J. M. Fellous, M. E. Hasselmo, B. L.  
477 McNaughton, Phase precession and variable spatial scaling in a peri-  
478 odic attractor map model of medial entorhinal grid cells with realis-  
479 tic after-spike dynamics, *Hippocampus* 22 (4) (2012) 772–789 (2012).  
480 doi:10.1002/hipo.20939.
- 481 [19] A. Guanella, P. Verschure, A Model of Grid Cells Based on a Path In-  
482 tegration Mechanism, *Artificial Neural Networks –ICANN 2006* (2006).  
483 doi:10.1007/11840817.
- 484 [20] S. Kunkel, A. Morrison, P. Weidel, J. M. Eppler, A. Sinha, W. Schenck,  
485 M. Schmidt, S. B. Vennemo, J. Jordan, A. Peyser, D. Plotnikov,  
486 S. Graber, T. Fardet, D. Terhorst, H. Mrk, G. Trensche, A. Seeholzer,  
487 R. Deepu, J. Hahne, I. Blundell, T. Ippen, J. Schuecker, H. Bos, S. Diaz,  
488 E. Hagen, S. Mahmoudian, C. Bachmann, M. E. Lepperd, O. Bre-  
489 itwieser, B. Golosio, H. Rothe, H. Setareh, M. Djurfeldt, T. Schumann,  
490 A. Shusharin, J. Garrido, E. B. Muller, A. Rao, J. H. Vieites, H. E.  
491 Plesser, *Nest* 2.12.0 (Mar. 2017). doi:10.5281/zenodo.259534.  
492 URL <https://doi.org/10.5281/zenodo.259534>

- 493 [21] E. Jones, T. Oliphant, P. Peterson, et al., SciPy: Open source scientific  
494 tools for Python, [Online] (2001–).  
495 URL <http://www.scipy.org/>
- 496 [22] E. Izhikevich, Simple model of spiking neurons, IEEE Transactions  
497 on Neural Networks 14 (6) (2003) 1569–1572 (2003). arXiv:ArXiv,  
498 doi:10.1109/TNN.2003.820440.
- 499 [23] E. M. Izhikevich, Dynamical systems in neuroscience, MIT press, 2007  
500 (2007).
- 501 [24] B. G. Burton, M. N. Economo, G. J. Lee, J. A. White, Development of  
502 theta rhythmicity in entorhinal stellate cells of the juvenile rat, Journal  
503 of neurophysiology 100 (6) (2008) 3144–3157 (2008).
- 504 [25] F. Sargolini, M. Fyhn, T. Hafting, B. McNaughton, M. Witter,  
505 M. Moser, E. Moser, Conjunctive representation of position, direction,  
506 and velocity in entorhinal cortex, Science 312 (5774) (2006) 758–762  
507 (2006).
- 508 [26] D. Bush, N. Burgess, A Hybrid Oscillatory Interference/Continuous At-  
509 tractor Network Model of Grid Cell Firing, Journal of Neuroscience  
510 34 (14) (2014) 5065–5079 (2014). doi:10.1523/JNEUROSCI.4017-  
511 13.2014.
- 512 [27] M. E. Hasselmo, L. M. Giocomo, E. A. Zilli, Grid cell firing may  
513 arise from interference of theta frequency membrane potential oscilla-  
514 tions in single neurons, Hippocampus 17 (12) (2007) 1252–1271 (2007).  
515 doi:10.1002/hipo.20374.
- 516 [28] D. Derdikman, J. R. Whitlock, A. Tsao, M. Fyhn, T. Hafting, M.-B.  
517 Moser, E. I. Moser, Fragmentation of grid cell maps in a multicompart-  
518 ment environment, Nature Neuroscience (2009). doi:10.1038/nn.2396.
- 519 [29] B. Marcelin, Z. Liu, Y. Chen, A. S. Lewis, A. Becker, S. McClelland,  
520 D. M. Chetkovich, M. Migliore, T. Z. Baram, M. Esclapez, C. Bernard,  
521 Dorsoventral Differences in Intrinsic Properties in Developing CA1 Pyra-  
522 midal Cells, Journal of Neuroscience 32 (11) (2012) 3736–3747 (2012).  
523 doi:10.1523/JNEUROSCI.5870-11.2012.

- 524 [30] N. K. Kasabov. "Time-Space, Spiking Neural Networks and Brain-  
525 Inspired Artificial Intelligence", Springer, 7 (2018).
- 526 [31] Triplett, Marcus A., Lilach Avitan, and Geoffrey J. Goodhill. "Emer-  
527 gence of spontaneous assembly activity in developing neural networks  
528 without afferent input." *PLoS computational biology* 14.9 (2018):  
529 e1006421.
- 530 [32] Burak, Yoram, and Ila R. Fiete. "Accurate path integration in continu-  
531 ous attractor network models of grid cells." *PLoS computational biology*  
532 5.2 (2009): e1000291.
- 533 [33] Rumsey, Clifton C., and L. F. Abbott. "Equalization of synaptic effi-  
534 cacy by activity-and timing-dependent synaptic plasticity." *Journal of*  
535 *neurophysiology* 91.5 (2004): 2273-2280.
- 536 [34] Ulanovsky, Nachum. "Neuroscience: how is three-dimensional space en-  
537 coded in the brain?." *Current Biology* 21.21 (2011): R886-R888.
- 538 [35] Johnson, Adam, and A. David Redish. "Neural ensembles in CA3 tran-  
539 siently encode paths forward of the animal at a decision point." *Journal*  
540 *of Neuroscience* 27.45 (2007): 12176-12189.
- 541 [36] Santos-Pata, Diogo, and Paul FMJ Verschure. "Human vicarious trial  
542 and error is predictive of spatial navigation performance." *Frontiers in*  
543 *behavioral neuroscience* 12 (2018).

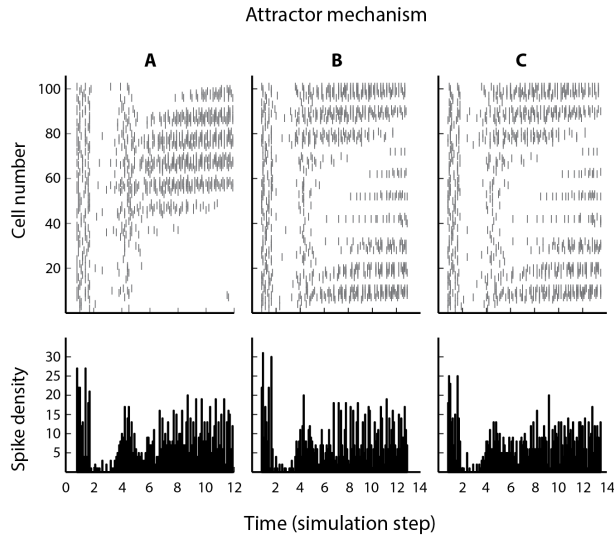


Figure S1: **Evidence of attraction at the simulation initial steps.** Every cell at each population (assemble) starts with random activity. The bump of activity is formed and attracted to a set of cells. A, B and C represents activity from population 1, 10 and 19, respectively.

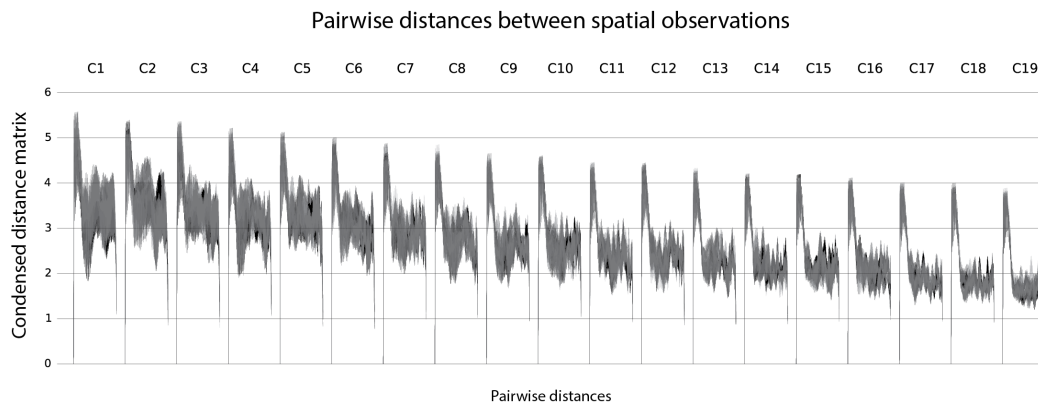


Figure S2: **Pairwise distances between spatial observations.** Gaussian kernel sigma of firing fields for ten cells at each condition is shown. Decrease of condensed distance matrix against pairwise distances from ventral (left) to dorsal (right) conditions.